

Coherent spin-1 dynamics encoded in the rotational states of ultracold molecules

Tom R. Hepworth,^{*} Daniel K. Ruttley,^{*} Fritz von Gierke,[†]

Philip D. Gregory, Alexander Guttridge, and Simon L. Cornish[‡]

*Department of Physics, Durham University, South Road, Durham, DH1 3LE, United Kingdom and
Joint Quantum Centre Durham-Newcastle, Durham University, South Road, Durham, DH1 3LE, United Kingdom*

(Dated: December 20, 2024)

The rotational states of ultracold polar molecules possess long radiative lifetimes, microwave-domain coupling, and tunable dipolar interactions. Coherent dynamics between pairs of rotational states have been used to demonstrate simple models of quantum magnetism and to manipulate quantum information stored as qubits. The availability of numerous rotational states has led to many proposals to implement more complicated models of quantum magnetism, higher-dimensional qudits, and intricate state networks as synthetic dimensions; however, these are yet to be experimentally realised. The primary issue limiting their implementation is the detrimental effect of the optical trapping environment on coherence, which is not easily mitigated for systems beyond two levels. To address this challenge, we investigate the applicability of magic-wavelength optical tweezer traps to facilitate *multi*transition coherence between rotational states. We demonstrate simultaneous second-scale coherence between three rotational states. Utilising this extended coherence, we perform multiparameter estimation using a generalised Ramsey sequence and demonstrate coherent spin-1 dynamics encoded in the rotational states. Our work paves the way to implementing proposed quantum simulation, computation, and metrology schemes that exploit the rich rotational structure of ultracold polar molecules.

Ultracold polar molecules possess vibrational, rotational, and hyperfine degrees of freedom which form a vast, low-energy, and experimentally accessible Hilbert space. With sufficient control, this complexity offers many avenues for developing quantum technologies [1] and exploring fundamental physics [2]. A particularly attractive degree of freedom is the ladder of rotational states. These states have long radiative lifetimes, are easily coupled with microwave radiation, and support controllable dipolar interactions. Therefore, they can be used to encode models of quantum magnetism [3–6], synthetic dimensions [7–10], and qudits [11–13]. However, for these applications it is crucial to decouple these internal degrees of freedom from the external environmental [14].

To date, rotational states of molecules have been used to study various spin-1/2 systems [15–17] and to encode qubits that can be prepared in maximally entangled Bell states [18–21]. Extending these studies beyond two-level systems is an outstanding challenge, primarily due to the coherence times that can be achieved for rotational state superpositions. Protocols such as dynamical decoupling [22, 23] can extend these coherence times for two-level systems, but these protocols are not easily generalised to n -level systems [24, 25].

Decoherence of rotational-state superpositions in molecules is primarily caused by the large differential polarisability between the states of the superposition. As a result, variations in the optical-trap intensity sampled

by the molecules lead to rapid dephasing [14, 26, 27]. Early approaches to minimise the differential polarisability (and resultant dephasing) used trapping light at a magic polarisation [26–29]. We have recently pioneered an alternative approach where the trapping light is at a magic wavelength [30]. This magic-wavelength light eliminates differential polarisability between two chosen molecular states to first order, with minimal to no higher order effects, enabling second-scale rotational coherence [31] and long-lived entanglement of pairs of individually trapped molecules [21].

In this work, we demonstrate how magic-wavelength traps can be used beyond two-level systems, extending the applications of ultracold molecules in quantum science. We use Ramsey interferometry to perform Hz-level spectroscopy, precisely determining the magic wavelength and its sensitivity to changes in laser frequency and intensity, for different rotational-state superpositions. We observe and explain small shifts in the optimum laser frequency for each superposition.

With this understanding, we engineer simultaneous second-scale coherence between three rotational levels realising, for the first time, coherent spin-1 dynamics encoded in the rotational states of ultracold molecules. As a demonstration of a quantum-science application that utilises this spin-1 system, we generalise a Ramsey sequence to the three levels and perform quantum multiparameter estimation [32, 33].

Theory of magic-wavelength trapping

Generally, the polarisability of a diatomic molecule is anisotropic. Its response to light can be described by components of the molecule-frame polarisability which

^{*} These authors contributed equally to this work.

[†] Present address: Institut für Quantenoptik, Leibniz Universität Hannover, 30167 Hannover, Germany

[‡] s.l.cornish@durham.ac.uk

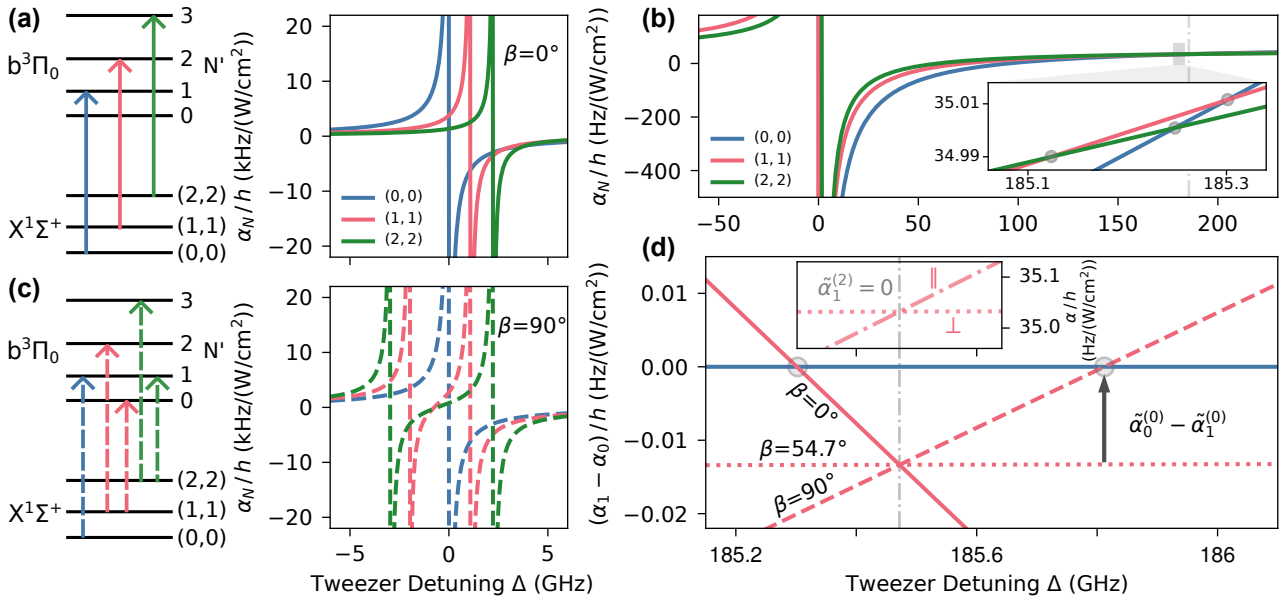


FIG. 1. **Origin of magic-wavelength trapping.** Polarisabilities of the lowest three stretched rotational states of RbCs molecules for wavelengths in the vicinity of transitions to the lowest vibrational level of $b^3\Pi$. (a) Left: the allowed transitions, when $\beta = 0^\circ$, to states with rotational quantum number N' in the electronically excited manifold $b^3\Pi_0$. Right: the associated poles in polarisability due to these allowed transitions. (b) The polarisabilities over a broad range of tweezer detuning Δ for $\beta = 0^\circ$. The grey vertical line indicates where $\tilde{\alpha}_1^{(2)} = 0$. The inset displays a region around 185.2 GHz where the polarisabilities for all three states are almost equal simultaneously. The crossing points (circles) correspond to the exact magic conditions for each pair of states. (c) The allowed transitions and polarisability poles for $\beta = 90^\circ$. (d) The differential polarisability $(\alpha_1 - \alpha_0)$ for various laser polarisations; the magic conditions are again indicated by circles. The grey vertical line again indicates where $\tilde{\alpha}_1^{(2)} = 0$; the inset highlights that this occurs when $\alpha_{\parallel} (\equiv \parallel)$ is tuned to be equal to $\alpha_{\perp} (\equiv \perp)$. At this detuning the polarisabilities of (0,0) and (1,1) are not equal due to a small difference in $\tilde{\alpha}^{(0)}$ between the states.

are parallel (α_{\parallel}) and perpendicular (α_{\perp}) to the internuclear axis. Broadly speaking, if these components are not equal, different molecular states (with different wavefunctions) experience different polarisabilities and, hence, are prone to rapid dephasing [34]. In the ideal case, the differential light shifts can be eliminated for all rotational-state superpositions by tuning the polarisability to be isotropic (that is, finding a wavelength where $\alpha_{\parallel} = \alpha_{\perp}$). Such wavelengths can be found in the vicinity of an electronic transition that, due to symmetry, only tunes α_{\parallel} [30]. We have previously used this approach to realise second-scale coherence between *two* rotational levels in a magic-wavelength trap [21, 31]. However, this simple idealised picture neglects subtle effects stemming from the rotational structure in the electronic transitions used to tune the polarisability. Such effects are negligible in most far-detuned optical traps, but are resolvable in a magic-wavelength trap and influence the optimal wavelength choice when engineering a trap that maximises the coherence on multiple rotational-state superpositions simultaneously.

The magic-wavelength trap we use for ground-state $^{87}\text{Rb}^{133}\text{Cs}$ molecules operates at a wavelength of 1145.3 nm and is detuned approximately +185 GHz from a nominally-forbidden transition to the ground vibrational level ($v' = 0$) of $b^3\Pi$ [21, 31]. This transition has

a linewidth of 14.1(3) kHz [35], so the trap is effectively far detuned and loss due to photon scattering is negligible. We prepare the molecules in the spin-stretched rotational states $N = 0, 1, 2$ with projection $M_N = N$. We explicitly label these states as (N, M_N) . We reference the detuning Δ of the trap light relative to the frequency of the transition ($X^1\Sigma^+, v = 0, N = 0, M_N = 0$) \rightarrow ($b^3\Pi_0, v' = 0, N' = 1, M'_N = 0$). The overall lab-frame polarisabilities α_N for molecules prepared in these states are shown in Fig. 1 across various detuning ranges and for laser polarisation angles parallel ($\beta = 0^\circ$) and perpendicular ($\beta = 90^\circ$) to the quantisation axis defined by an applied magnetic field.

In Fig. 1(a) we show the molecule response to the light when $\beta = 0^\circ$. In this case, the light can only address π transitions that conserve M_N . So for each spin-stretched state we have one accessible transition where $N' = N + 1$, with each transition occurring at a different laser frequency due to the anharmonic spacing of the rotational levels. As a consequence, the associated pole in the polarisability is shifted in frequency for each rotational state. As shown in Fig. 1(b), even at the much larger detuning ($\Delta \sim 185$ GHz) where the magic condition occurs, there are still small differences in the polarisability for each state at a given detuning. The inset shows a closeup of this region, highlighting the exact magic wavelengths for

each pair of rotational states (circles). Notably, these do not occur at the same laser frequency. Despite the absence of an exact magic condition for three states simultaneously, the difference in the polarisability across this ~ 200 MHz wide detuning window is very small ($\lesssim 0.1\%$). As we will demonstrate, the small scale of these deviations allows second-scale coherences on multiple rotational-state superpositions simultaneously.

Changing the laser polarisation gives further insight into how the polarisability is affected by the rotational structure and selection rules. In Fig. 1(c) we show the molecule response to the light when $\beta = 90^\circ$. Here, the light can address σ^\pm transitions that change M_N by ± 1 . For $N = 0$ the light still only drives transitions to the manifold $N' = 1$, but for $N > 0$ it now drives transitions to two manifolds with $N' = N \pm 1$. Again, the location of the poles depends on N , but the response is very different to the $\beta = 0^\circ$ case. Therefore, we expect the magic condition to also be slightly polarisation dependent.

To model the polarisability it is useful to consider it decomposed into scalar and tensor contributions. Molecules in $N = 0$ only experience light shifts from scalar polarisability, due to their spherically symmetric angular distribution, while those in rotationally excited states are affected by both the scalar and tensor contributions. The polarisabilities, for our considered states with $M_N = N$, are described by the equation

$$\alpha_N(\Delta, \beta) = \tilde{\alpha}_N^{(0)}(\Delta) + \tilde{\alpha}_N^{(2)}(\Delta)C_N P_2(\cos \beta), \quad (1)$$

where $C_N \equiv -N/(2N + 3)$ and $P_2(x) \equiv (3x^2 - 1)/2$. The terms $\tilde{\alpha}_N^{(0)}, \tilde{\alpha}_N^{(2)}$ govern the magnitude of the scalar and tensor polarisability; these both depend on N due to the rotational structure presented in Fig. 1(a-c). We caution that these are not exactly equivalent to the scalar and tensor polarisabilities in far-detuned traps that have been used in our previous work [34] (Methods).

Since $\tilde{\alpha}_N^{(0)}$ and $\tilde{\alpha}_N^{(2)}$ depend on N , the detuning that exactly cancels the tensor component for a given state does not result in zero light shift relative to another state with different N . Figure 1(d) shows the differential polarisability between $N = 0$ and $N = 1$ around the magic condition for various β . When the tensor polarisability for $N = 1$ is nulled (grey vertical line), the differential polarisability becomes independent of the laser polarisation and is simply equal to $\tilde{\alpha}_{N=1}^{(0)} - \tilde{\alpha}_{N=0}^{(0)}$. To exactly match the polarisabilities of the states, it is therefore necessary to *introduce* a small tensor light shift to compensate this difference in the scalar polarisabilities. The angle of the polarisation β , via the factor $P_2(\cos \beta)$, dictates the magnitude and sign of $\tilde{\alpha}_N^{(2)}(\Delta)$ required and, hence, the magic detuning, Δ_{magic} . For $\beta \approx 54.7^\circ$, where $P_2(\cos \beta) = 0$, the tensor light shift only affects the polarisability via second-order terms which makes the magic condition inaccessible. In contrast, the magnitude of $P_2(\cos \beta)$ has maxima at $\beta = 0^\circ$ and 90° equal to 1 and $-1/2$, respectively. These polarisations therefore allow an exact magic condition between two rotational states to be found close

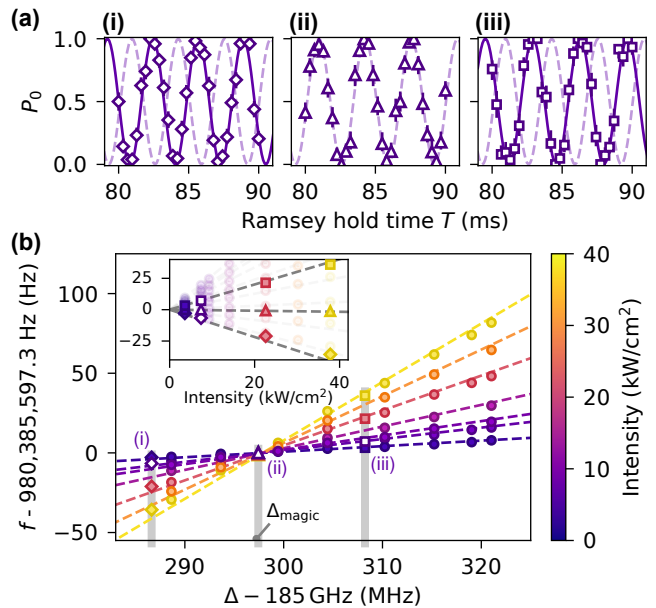


FIG. 2. **Measurements of the light shift of the transition $(0,0) \rightarrow (1,1)$, with $\beta = 0^\circ$, around the magic condition.** (a) Typical Ramsey fringes for three different Δ , indicated, in (b) by the vertical grey lines. Dashed and solid lines are the fit of the Ramsey fringes. The dashed fit line of the trap in (ii) is superimposed on the other plots to highlight the phase slip at $T \sim 80$ ms due to the different transition frequencies. (b) Fitted transition frequencies as a function of Δ for many trap intensities I . The inset shows the same data but against I for many Δ to demonstrate linearity. The points in the grey shaded regions correspond to the highlighted detunings in the inset. The hollow points correspond to the fitted frequency of the fringes shown in (a). The dashed lines show the fitted model (Methods). Error bars in all panels are 1σ confidence intervals.

est to each side of the isotropic detuning. Overall, the detuning which nulls the differential polarisability depends on both the states of the rotational superposition and β . We stress, however, this is only when an *exact* magic condition is desired for a given superposition. Due to the small scales associated with these tensor compensations, a near-magic trap will still show long coherence times, and can be optimised over many superpositions.

Finding the magic conditions

We perform two-level Ramsey spectroscopy with Hz-level sensitivity to measure the small shifts in the magic detuning associated with changing the rotational state superposition and tweezer polarisation. We prepare equal superpositions of pairs of rotational states using near-resonant microwave pulses and then allow these superpositions to freely evolve for time T before mapping the accumulated relative phase onto state populations (Methods). To measure the state populations, we map

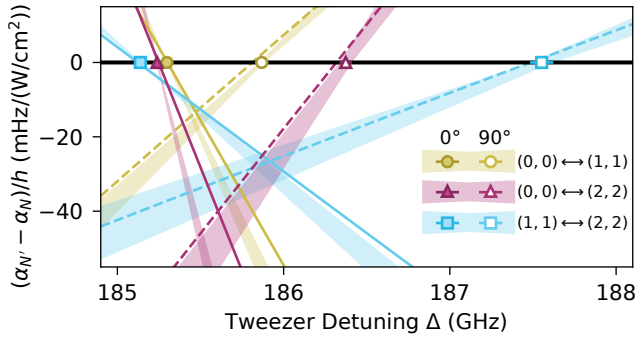


FIG. 3. **Magic-detuning and sensitivity for the rotational-state superpositions shown in the legend.** Points mark the fitted magic detuning, Δ_{magic} , for each transition and tweezer polarisation with 1σ error bars. The light shaded region indicates the 1σ uncertainty region of the measured sensitivity, k . The solid and dashed lines are the differential polarisabilities, for $\beta = 0^\circ$ and 90° respectively, obtained by fitting our polarisability model to the data (Methods).

each rotational state to a distinct spatial configuration of atoms [36]. This allows us to correct for errors, such as molecule loss, with postselection. Figure 2(a) shows examples of such Ramsey measurements. Here, we prepare molecules in a superposition of $(0, 0)$ and $(1, 1)$, and the polarisation of the trapping light is set to be along the quantisation axis ($\beta = 0^\circ$) (Methods). Oscillations in the population P_0 of the state $(0, 0)$ occur at a frequency equal to the detuning of the microwaves from the light-shifted transition frequency, generally denoted f , of $(0, 0) \rightarrow (1, 1)$. The three panels are for different frequencies of trapping light, indicated by the grey vertical lines in Fig. 2(b). The small differential light shifts enable long free-evolution times without decoherence, allowing us to resolve transition frequency shifts with Hz-level precision. To find the magic detuning, we repeat the Ramsey procedure to find f for traps of different intensities I and detunings Δ . Figure 2(b) shows these measurements. The main panel shows the dependence of f on Δ for various I (indicated with the colour scale). At the magic detuning, Δ_{magic} , the light shift of the transition is eliminated. This is seen at the points indicated with (ii) where f is constant for different values of I . The inset shows the same data but plotted as f against I for various Δ , to show linearity. At Δ_{magic} , f is independent of I and the points previously indicated with (ii) are now more easily seen as the horizontal line. We fit the data with the equation $f = f_0 + k(\Delta - \Delta_{\text{magic}})I$ to extract the free-space transition frequency $f_0 = 980, 385, 597.3(2)$ Hz, the magic detuning $\Delta_{\text{magic}} = 185.2980(7)$ GHz, and the sensitivity constant $k = 98(3)$ mHz/MHz/(kW/cm²).

We perform similar measurements for superpositions of $(1, 1)$ and $(2, 2)$ as well as superpositions of $(0, 0)$ and $(2, 2)$, for two different trap polarisations, $\beta = 0^\circ$ and 90° (Methods). Figure 3 shows the results from these measurements. For each transition, the measured value

of Δ_{magic} is shown by the point and the measured value of k is displayed as the corresponding shaded region. For the case of $\beta = 90^\circ$ we must include an additional *hyperpolarisability* term in our fitting function. This is caused by off-diagonal elements in the tensor polarisability operator that exist for non-zero β , which couple the stretched states to other nearby hyperfine states [34]. The energy shift of a state from this off-diagonal coupling scales quadratically with intensity and quadratically with detuning from where $\tilde{\alpha}^{(2)} = 0$ (Methods).

The dependence of the molecular polarisability on the wavelength and polarisation of the trap light is well described by our model (Eq. (1) and Methods). The solid (dashed) lines in Fig. 3 show the expected polarisability of the states (N, M_N) when $\beta = 0^\circ$ ($\beta = 90^\circ$). The majority of the parameters in our model are fixed to the molecular constants in Refs [35, 37] and the measured background value of α_\perp (Methods). We fit only the rotational constant of the excited state and the background value of α_\parallel (Methods). This model allows us to predict the magic detunings and sensitivities of other rotational-state superpositions.

Simultaneous second-scale coherence

Examining the locations of Δ_{magic} in Fig. 3, we see that the magic detunings when $\beta = 0^\circ$ lie in a window between $\Delta = 185.1$ and 185.4 GHz. At our usual trapping intensity of $I = 4.6(3)$ kW/cm², the most sensitive superposition, $(0, 0)$ and $(2, 2)$, is expected to have a sensitivity to laser-frequency deviations of just ~ 510 mHz/MHz, which, even with our laser-frequency stability of $\sigma_\Delta = 80(20)$ kHz [21], gives a $T_2^* \approx 4$ s. The peak sensitivity of each superposition to variations in sampled intensity across this window is $\lesssim 13$ Hz/(kW/cm²). Therefore, with sufficiently low variation in the sampled intensity of the molecule, we expect to find a detuning that will simultaneously support second-scale coherent superpositions for all three rotational state combinations.

To probe the rotational coherence across the window spanning the magic detunings we again use Ramsey interferometry, now with a hold time of $T \sim 500$ ms. We set the detuning of the microwaves from the one-photon transitions to ~ 100 Hz and use trap intensities of $I = 4.6(3)$ kW/cm². Figure 4(a) shows the contrast C of the Ramsey oscillations as a function of the tweezer detuning Δ . For all three cases, the observed detuning-dependence of the contrast is consistent with tweezer intensity noise [21] with a standard deviation of $0.65(4)\%$, as shown by the lines (Methods). The different widths of the features reflect the different sensitivities reported in Fig. 3. This level of intensity noise allows us to engineer simultaneous second-scale coherence for all three superpositions. To do this, we set $\Delta \approx 185.26$ GHz [Fig. 4(a), grey line]. Here, we expect that the T_2^* time for each superposition exceeds 1.5 s (Methods). In Fig. 4(b), we show Ramsey fringes for the three superpositions using a

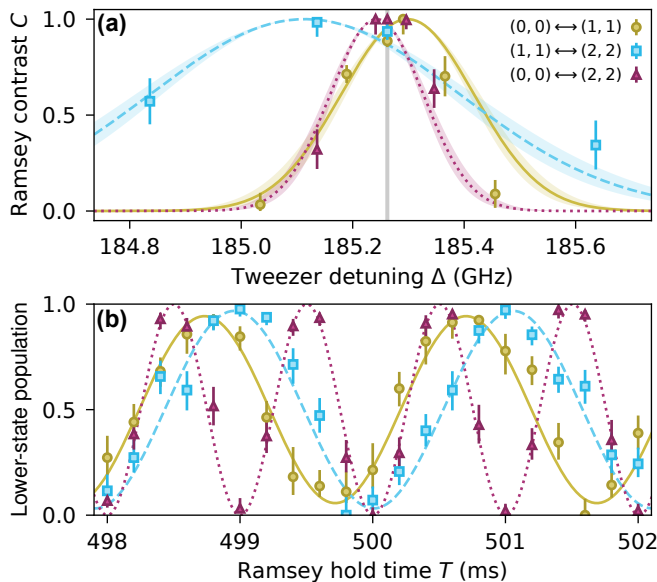


FIG. 4. **Second-scale coherence on all three rotational-state superpositions.** (a) Ramsey fringe contrast C as a function of tweezer detuning Δ for each superposition at $\beta = 0^\circ$. The lines are the results of a model fitted to all the measurements with a single free parameter corresponding to the Gaussian intensity noise (Methods). (b) Ramsey oscillations for the three superpositions at a detuning of ~ 185.26 GHz, indicated by the grey vertical line in (a). Error bars in both panels are 1σ confidence intervals.

Ramsey hold time $T \sim 500$ ms. In all cases we see close to full contrast fringes, demonstrating long-lived coherence for all three rotational-state superpositions at this detuning. The frequency is twice as fast for the superposition of $(0,0)$ and $(2,2)$ as both microwave fields used to drive the two-photon transition were detuned.

Operating at the optimum detuning reported in Fig. 4 allows us to prepare a highly coherent quantum superposition of all three rotational states, effectively encoding a spin-1 system in the molecule. We use the ensuing dynamics to perform quantum multiparameter estimation [32, 33]; a technique that has important applications in quantum metrology [38]. Explicitly, we use a generalised Ramsey sequence to precisely measure the energies of the three states. We exploit the non-trivial interference of the phases accumulated by the states to produce a complicated interference pattern which is simultaneously sensitive to detunings of both microwave fields from the transition frequencies.

Figure 5(a) illustrates our generalised Ramsey sequence. First, we use microwave pulses to transfer molecules from the state $(0,0)$ to an equal superposition of the three states (Methods). We detune the microwaves from the one-photon transitions $(0,0) \rightarrow (1,1)$ and $(1,1) \rightarrow (2,2)$ by $\delta_{01} \approx +100$ Hz and $\delta_{12} \approx -150$ Hz, respectively. We allow the superposition to evolve for time T and then perform a sequence of microwave pulses which maps the resulting phases in the superposition onto

the populations of all states (Methods). To measure the state populations, we extend the multistate readout scheme in Ref. [36] to three states. Examples of atomic configurations obtained with this readout scheme are shown in Fig. 5(b). In Fig. 5(c), we show the state populations after the generalised Ramsey sequence as a function of T . The coherence between the three states is seen by the quasi-periodic zero occupation of each state, which is evident even at $T \sim 500$ ms. This simple metric of coherence is directly observable due to our multistate readout scheme; this contrasts to cases where multistate coherence is mapped onto a single measured observable [39, 40]. The non-trivial fringes in Fig. 5(c) are described well by an analytical model, shown by the solid lines, which we use to extract the microwave detunings (Methods). Using the whole interference pattern, we find $\delta_{01} = 98.11(2)$ Hz and $\delta_{12} = -149.51(2)$ Hz.

This measurement is remarkably sensitive due to quantum interference between the three states that is only possible due to their mutual coherence. We characterise this gain in sensitivity by computing the quantum Fisher information matrix for the equal-superposition state (Methods). This quantity, via the Cramér-Rao bound, sets the fundamental limit on the achievable measurement uncertainty of parameters encoded in a quantum state [32, 33]. For the equal superposition state, an optimal projective measurement requires only 3/4 of the number of measurements to achieve the same uncertainty on both parameters in this three-level interferometer compared to performing two rounds of two-level Ramsey interferometry (Methods). Further, the posterior distribution for the two parameters, when measuring in discrete time windows, has far fewer nearby modes of high probability than the two-level Ramsey measurement. This is due to the complicated interference pattern and makes the fitting procedure easier. In future, we expect that similar procedures could increase the data-acquisition rate and decrease the uncertainty on measured values when performing spectroscopy of multilevel systems.

Outlook

The generalised three-level Ramsey sequence demonstrates the encoding of coherent spin-1 dynamics in the rotational structure of molecules. Crucially we have shown that our magic-wavelength trapping supports second-scale coherence for all three rotational state superpositions simultaneously. The measured T_2^* times are far longer than the timescale associated with dipolar interactions between molecules for typical tweezer or lattice spacings [18–21]. Our work therefore paves the way for studies of interacting many-body quantum systems with large internal degrees of freedom. For example, a lattice of three-level molecules, in the presence of interactions, could represent a system of spin-1/2 hard-core bosons using the mapping $|\downarrow\rangle \equiv (0,0)$, $|\otimes\rangle \equiv (1,1)$, and

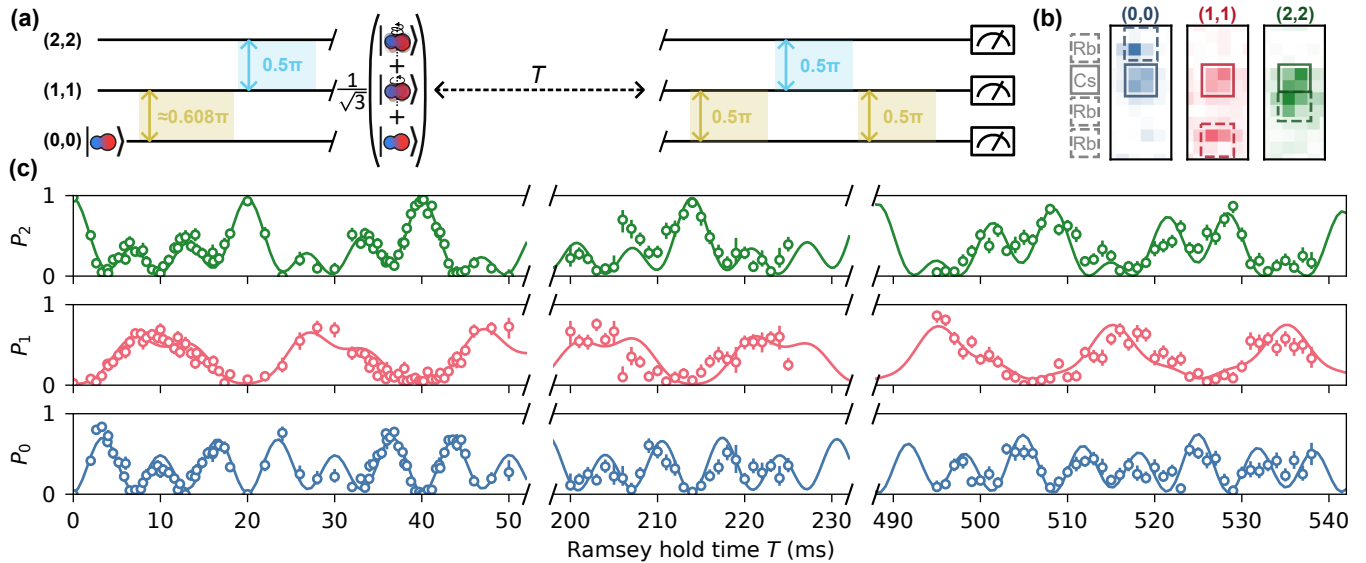


FIG. 5. **Three-level generalised Ramsey sequence.** (a) The microwave pulse scheme used in the measurement. The molecules are prepared in the state (0,0). The initial two pulses then form an equal superposition of all (0,0), (1,1) and (2,2). The relative phases in the superposition then evolve for a Ramsey hold time, T . The final pulses map the phases accumulated to interference in the populations of the states, which are then measured. (b) Averaged fluorescence images showing the spatial configurations of the atoms following molecular dissociation that correspond to each molecular state in the multistate readout procedure. (c) Populations of three states as a function of Ramsey hold time, T . Error bars are 1σ confidence intervals. The whole interference pattern is fitted with an analytic model assuming no decoherence, shown with the solid lines.

$|\uparrow\rangle \equiv (2, 2)$. Here, $|\downarrow\rangle$ and $|\uparrow\rangle$ would represent the bosonic spin states and $|\otimes\rangle$ a hole. The spin states would directly couple only to the hole state, allowing for representations of bosonic tunnelling and the study of interesting topological effects [41].

Looking further ahead, our model predicts that the techniques demonstrated here can be readily extended to systems of more states. For example, second-scale coherence on all pairs of stretched rotational states up to $N = 10$ would require less than an order of magnitude improvement in the intensity noise. This would open the door to studies of many-body $SU(N)$ systems [6, 42] and interacting high-dimensional synthetic dimensions [7–10]. Additionally, the long-lived coherence between the rotational states could be exploited to densely encode quantum information in order to form interacting qudits [11–13, 43] or quantum memories in hybrid quantum systems [44–46].

References

- [1] Cornish, S. L., Tarbutt, M. R. & Hazzard, K. R. A. Quantum computation and quantum simulation with ultracold molecules. *Nat. Phys.* **20**, 730 (2024).
- [2] DeMille, D., Hutzler, N. R., Rey, A. M. & Zelevinsky, T. Quantum sensing and metrology for fundamental physics with molecules. *Nat. Phys.* **20**, 741 (2024).
- [3] Barnett, R., Petrov, D., Lukin, M. & Demler, E. Quantum magnetism with multicomponent dipolar molecules in an optical lattice. *Phys. Rev. Lett.* **96**, 190401 (2006).
- [4] Gorshkov, A. V. *et al.* Tunable superfluidity and quantum magnetism with ultracold polar molecules. *Phys. Rev. Lett.* **107**, 115301 (2011).
- [5] Hazzard, K. R. A., Manmana, S. R., Foss-Feig, M. & Rey, A. M. Far-from-equilibrium quantum magnetism with ultracold polar molecules. *Phys. Rev. Lett.* **110**, 075301 (2013).
- [6] Mukherjee, B., Hutson, J. M. & Hazzard, K. $SU(N)$ magnetism with ultracold molecules. *New J. Phys.* (2024).
- [7] Sundar, B., Gadway, B. & Hazzard, K. R. A. Synthetic dimensions in ultracold polar molecules. *Sci. Rep.* **8**, 3422 (2018).
- [8] Sundar, B., Thibodeau, M., Wang, Z., Gadway, B. & Hazzard, K. R. A. Strings of ultracold molecules in a synthetic dimension. *Phys. Rev. A* **99**, 013624 (2019).
- [9] Feng, C., Manetsch, H., Rousseau, V. G., Hazzard, K. R. A. & Scalettar, R. Quantum membrane phases in synthetic lattices of cold molecules or Rydberg atoms. *Phys. Rev. A* **105**, 063320 (2022).
- [10] Cohen, M., Casebolt, M., Zhang, Y., Hazzard, K. R. A. & Scalettar, R. Classical analog of quantum models in synthetic dimensions. *Phys. Rev. A* **109**, 013303 (2024).
- [11] Albert, V. V., Covey, J. P. & Preskill, J. Robust encoding of a qubit in a molecule. *Phys. Rev. X* **10**, 031050 (2020).
- [12] Wang, Y., Hu, Z., Sanders, B. C. & Kais, S. Qudits and high-dimensional quantum computing. *Front. Phys.* **8**, 589504 (2020).
- [13] Sawant, R. *et al.* Ultracold polar molecules as qudits. *New J. Phys.* **22**, 013027 (2020).
- [14] Langen, T., Valtolina, G., Wang, D. & Ye, J. Quantum state manipulation and cooling of ultracold molecules. *Nat. Phys.* **20**, 702 (2024).
- [15] Yan, B. *et al.* Observation of dipolar spin-exchange in-

- interactions with lattice-confined polar molecules. *Nature* **501**, 521 (2013).
- [16] Li, J.-R. *et al.* Tunable itinerant spin dynamics with polar molecules. *Nature* **614**, 70 (2023).
- [17] Christakis, L. *et al.* Probing site-resolved correlations in a spin system of ultracold molecules. *Nature* **614**, 64 (2023).
- [18] Bao, Y. *et al.* Dipolar spin-exchange and entanglement between molecules in an optical tweezer array. *Science* **382**, 1138 (2023).
- [19] Holland, C. M., Lu, Y. & Cheuk, L. W. On-demand entanglement of molecules in a reconfigurable optical tweezer array. *Science* **382**, 1143 (2023).
- [20] Picard, L. R. B. *et al.* Entanglement and iSWAP gate between molecular qubits. *Nature* (2024).
- [21] Ruttley, D. K., Hepworth, T. R., Guttridge, A. & Cornish, S. L. Long-lived entanglement of molecules in magic-wavelength optical tweezers (2024). URL <https://arxiv.org/abs/2408.14904>. arXiv:2408.14904 [physics.atom-ph].
- [22] Haeberlen, U. & Waugh, J. S. Coherent averaging effects in magnetic resonance. *Phys. Rev.* **175**, 453 (1968).
- [23] Viola, L. & Knill, E. Robust dynamical decoupling of quantum systems with bounded controls. *Phys. Rev. Lett.* **90**, 037901 (2003).
- [24] Yuan, X. *et al.* Preserving multilevel quantum coherence by dynamical decoupling. *Phys. Rev. A* **106**, 022412 (2022).
- [25] da Silva, A. H., Napolitano, R. d. J., Fanchini, F. F. & Bellomo, B. Time-dependent Rabi frequencies to protect quantum operations on an atomic qutrit by continuous dynamical decoupling. *Phys. Rev. A* **109**, 032611 (2024).
- [26] Burchesky, S. *et al.* Rotational coherence times of polar molecules in optical tweezers. *Phys. Rev. Lett.* **127**, 123202 (2021).
- [27] Park, A. J. *et al.* Extended rotational coherence of polar molecules in an elliptically polarized trap. *Phys. Rev. Lett.* **131**, 183401 (2023).
- [28] Seeßelberg, F. *et al.* Extending rotational coherence of interacting polar molecules in a spin-decoupled magic trap. *Phys. Rev. Lett.* **121**, 253401 (2018).
- [29] Tobias, W. G. *et al.* Reactions between layer-resolved molecules mediated by dipolar spin exchange. *Science* **375**, 1299 (2022).
- [30] Guan, Q., Cornish, S. L. & Kotochigova, S. Magic conditions for multiple rotational states of alkali molecules in optical lattices. *Phys. Rev. A* **103**, 043311 (2021).
- [31] Gregory, P. D. *et al.* Second-scale rotational coherence and dipolar interactions in a gas of ultracold polar molecules. *Nat. Phys.* **20**, 415 (2024).
- [32] Demkowicz-Dobrzański, R., Górecki, W. & Guţă, M. Multi-parameter estimation beyond quantum Fisher information. *J. Phys. A* **53**, 363001 (2020).
- [33] Liu, J., Yuan, H., Lu, X.-M. & Wang, X. Quantum Fisher information matrix and multiparameter estimation. *J. Phys. A* **53**, 023001 (2019).
- [34] Gregory, P. D., Blackmore, J. A., Aldegunde, J., Hutson, J. M. & Cornish, S. L. ac Stark effect in ultracold polar $^{87}\text{Rb}^{133}\text{Cs}$ molecules. *Phys. Rev. A* **96**, 021402 (2017).
- [35] Das, A. *et al.* High-resolution spectroscopy of the $X^1\Sigma^+ - b^3\Pi_0$ transitions in ultracold $^{87}\text{Rb}^{133}\text{Cs}$ molecules (in preparation).
- [36] Ruttley, D. K., Guttridge, A., Hepworth, T. R. & Cornish, S. L. Enhanced quantum control of individual ultracold molecules using optical tweezer arrays. *PRX Quantum* **5**, 020333 (2024).
- [37] Gregory, P. D. *et al.* Sticky collisions of ultracold RbCs molecules. *Nat. Commun.* **10**, 3104 (2019).
- [38] Albarelli, F., Barbieri, M., Genoni, M. & Gianani, I. A perspective on multiparameter quantum metrology: From theoretical tools to applications in quantum imaging. *Phys. Lett. A* **384**, 126311 (2020).
- [39] Dive, B., Koukoulekidis, N., Mousafeiris, S. & Mintert, F. Characterization of multilevel quantum coherence without ideal measurements. *Phys. Rev. Res.* **2**, 013220 (2020).
- [40] Corfield, O. *et al.* Certifying multilevel coherence in the motional state of a trapped ion. *PRX Quantum* **2**, 040359 (2021).
- [41] Wellnitz, D. *et al.* Emergent interaction-induced topology in Bose-Hubbard ladders (2024). URL <https://arxiv.org/abs/2409.05109>. arXiv:2409.05109 [cond-mat.quant-gas].
- [42] Ciavarella, A. N. & Bauer, C. W. Quantum simulation of SU(3) lattice Yang-Mills theory at leading order in large- N_c expansion. *Phys. Rev. Lett.* **133**, 111901 (2024).
- [43] Roy, T., Li, Z., Kapit, E. & Schuster, D. Two-qutrit quantum algorithms on a programmable superconducting processor. *Phys. Rev. Appl.* **19**, 064024 (2023).
- [44] Wang, K., Williams, C. P., Picard, L. R. B., Yao, N. Y. & Ni, K.-K. Enriching the quantum toolbox of ultracold molecules with Rydberg atoms. *PRX Quantum* **3**, 030339 (2022).
- [45] Zhang, C. & Tarbutt, M. R. Quantum computation in a hybrid array of molecules and Rydberg atoms. *PRX Quantum* **3**, 030340 (2022).
- [46] Guttridge, A. *et al.* Observation of Rydberg blockade due to the charge-dipole interaction between an atom and a polar molecule. *Phys. Rev. Lett.* **131**, 013401 (2023).
- [47] Brieger, M. Stark effect, polarizabilities and the electric dipole moment of heteronuclear diatomic molecules in $^1\Sigma$ states. *Chem. Phys.* **89**, 275 (1984).
- [48] Bonin, K. D. & Kresin, V. V. *Electric-dipole polarizabilities of atoms, molecules and clusters* (World Scientific, Singapore, 1997).
- [49] Neyenhuis, B. *et al.* Anisotropic polarizability of ultracold polar $^{40}\text{K}^{87}\text{Rb}$ molecules. *Phys. Rev. Lett.* **109**, 230403 (2012).
- [50] Grimm, R., Weidemüller, M. & Ovchinnikov, Y. B. Optical dipole traps for neutral atoms. *Adv. At. Mol. Opt. Phys.* **42**, 95 (2000).
- [51] Kotochigova, S. *et al.* Rotational magic conditions for ultracold molecules in the presence of Raman and Rayleigh scattering. *New J. Phys.* **26**, 063025 (2024).
- [52] Blackmore, J. A., Gregory, P. D., Hutson, J. M. & Cornish, S. L. Diatomic-py: A Python module for calculating the rotational and hyperfine structure of $^1\Sigma$ molecules. *Comput. Phys. Commun.* **282**, 108512 (2023).
- [53] Brooks, R. V. *et al.* Preparation of one ^{87}Rb and one ^{133}Cs atom in a single optical tweezer. *New J. Phys.* **23**, 065002 (2021).
- [54] Spence, S., Brooks, R. V., Ruttley, D. K., Guttridge, A. & Cornish, S. L. Preparation of ^{87}Rb and ^{133}Cs in the motional ground state of a single optical tweezer. *New J. Phys.* **24**, 103022 (2022).
- [55] Ruttley, D. K. *et al.* Formation of ultracold molecules by merging optical tweezers. *Phys. Rev. Lett.* **130**, 223401 (2023).

- [56] Ammenwerth, M. *et al.* Realization of a fast triple-magic all-optical qutrit in strontium-88 (2024). URL <https://arxiv.org/abs/2411.02869>. arXiv:2411.02869 [physics.atom-ph].
- [57] Kaufman, A. M., Lester, B. J. & Regal, C. A. Cooling a single atom in an optical tweezer to its quantum ground state. *Phys. Rev. X* **2**, 041014 (2012).
- [58] Thompson, J. D., Tiecke, T. G., Zibrov, A. S., Vuletić, V. & Lukin, M. D. Coherence and Raman sideband cooling of a single atom in an optical tweezer. *Phys. Rev. Lett.* **110**, 133001 (2013).
- [59] Albrecht, B. *et al.* Fictitious magnetic-field gradients in optical microtraps as an experimental tool for interrogating and manipulating cold atoms. *Phys. Rev. A* **94**, 061401 (2016).
- [60] Kuhr, S. *et al.* Coherence properties and quantum state transportation in an optical conveyor belt. *Phys. Rev. Lett.* **91**, 213002 (2003).
- [61] Barakhshan, P. *et al.* Portal for high-precision atomic data and computation (version 2.0). [Online] (2022). URL <https://www.udel.edu/atom>.
- [62] Savard, T. A., O'Hara, K. M. & Thomas, J. E. Laser-noise-induced heating in far-off resonance optical traps. *Phys. Rev. A* **56**, R1095 (1997).
- [63] Buchner, J. Nested sampling methods. *Stat. Surv.* **17**, 169 (2023).
- [64] Buchner, J. UltraNest - a robust, general purpose Bayesian inference engine. *J. Open Source Softw.* **6**, 3001 (2021).
- [65] Valeri, M. *et al.* Experimental multiparameter quantum metrology in adaptive regime. *Phys. Rev. Res.* **5**, 013138 (2023).
- [66] Gregory, P. D., Aldegunde, J., Hutson, J. M. & Cornish, S. L. Controlling the rotational and hyperfine state of ultracold $^{87}\text{Rb}^{133}\text{Cs}$ molecules. *Phys. Rev. A* **94**, 041403(R) (2016).

METHODS

Model of the polarisability near the magic-wavelength

The dynamic polarisability of a diatomic molecule is generally anisotropic. When the light is sufficiently far detuned that rotational structure in the transitions can be ignored, the lab-frame polarisability α_{N,M_N} for a $^1\Sigma$ diatomic molecule in a given rotational state (N, M_N) can be approximated by [47, 48]

$$\alpha_{N,M_N}(\beta) = \alpha^{(0)} + C_{N,M_N} \alpha^{(2)} P_2(\cos \beta), \quad (2)$$

where $C_{N,M_N} \equiv [N(N+1) - 3M_N^2]/[(2N+3)(2N-1)]$, and β is the angle of the laser polarisation relative to the quantisation axis. The terms $\alpha^{(0)}$ and $\alpha^{(2)}$ quantify the scalar and tensor polarisabilities and are often referred to the *isotropic* and *anisotropic* polarisabilities, respectively. They are related to the molecule-frame polarisabilities in the directions parallel (α_{\parallel}) and perpendicular (α_{\perp}) to the bond axis such that

$$\alpha^{(0)} = \frac{1}{3}(\alpha_{\parallel} + \alpha_{\perp}), \quad (3)$$

$$\alpha^{(2)} = \frac{2}{3}(\alpha_{\parallel} - \alpha_{\perp}). \quad (4)$$

The polarisabilities $\alpha^{(0)}, \alpha^{(2)}$ (and $\alpha_{\parallel}, \alpha_{\perp}$) have a dependence on N but this is typically very small and safely neglected [34, 49]. However, we have shown that the N dependence of these polarisabilities becomes detectable for molecules in our magic-wavelength trap.

We calculate the polarisability of the molecules in response to the magic-wavelength trap by assuming background polarisabilities $\alpha_{\parallel}^{\text{bkgd}}$ and $\alpha_{\perp}^{\text{bkgd}}$ (which give rise to background values $\alpha_{\text{bkgd}}^{(0)}$ and $\alpha_{\text{bkgd}}^{(2)}$ through Eqs (3) & (4)) arising from all far-detuned electronic transitions. The remaining electronic transitions to the $b^3\Pi$ potential give rise to additional terms of the form $(3\pi c^2 \Gamma_{v'})/(2\omega^3 \Delta)$ [50] where c is the speed of light, $\Gamma_{v'}$ is the linewidth of the transition to a given vibrational state, ω is the transition frequency, and Δ is the detuning of the light from the transition. We include rotational structure in the model by summing over allowed π, σ^{\pm} transitions corresponding to a change in the rotational angular momentum $\Delta N = 0, \pm 1$ respectively. The value of M_N in the ground state together with the polarisation of the trap light dictates the degree to which these transitions contribute to the polarisability. The total polarisability in the magic-wavelength trap, assuming linearly polarised light, is therefore given by

$$\begin{aligned} \alpha_{N,M_N}(\beta) &= \alpha_{\text{bkgd}}^{(0)} + C_{N,M_N} \alpha_{\text{bkgd}}^{(2)} P_2(\cos \beta) \\ &- \sum_{v',N'} \frac{3\pi c^2 \Gamma_{v'}}{2\omega^3 \Delta_{v',N'}} \left(\frac{d_{\pm}^2}{2} \sin^2 \beta + \frac{d_{\pm}^2}{2} \sin^2 \beta + \frac{d_0^2}{2} \cos^2 \beta \right), \end{aligned} \quad (5)$$

where d_0, d_{\pm} correspond to the dipole moment for π, σ^{\pm} transitions respectively, and $\Delta_{v',N'}$ is the detuning from the vibrational and rotational level v', N' of $b^3\Pi$. Note that here we have assumed that the far-detuned approximation is valid for all transitions contributing to the background polarisabilities, $\alpha_{\text{bkgd}}^{(0)}$ and $\alpha_{\text{bkgd}}^{(2)}$, but not for the contribution from the nearest $b^3\Pi$ transitions.

Evaluating the term in parentheses in Eq. (5) has been done for $M_N = 0$ in Ref. [30], and for arbitrary M_N in Ref. [51].

We reproduce parts of those equations here for completeness. The total polarisability in the lab-frame is

$$\begin{aligned} \alpha_{N,M_N}(\beta) &= \alpha_{\text{bkgd}}^{(0)} + C_{N,M_N} \alpha_{\text{bkgd}}^{(2)} P_2(\cos \beta) \\ &- \sum_{v',N'} \frac{3\pi c^2 \Gamma_{v'}}{2\omega^2} \left(\frac{A_{N,M_N}}{\Delta_{v'} + L_N} + \frac{B_{N,M_N}}{\Delta_{v'} + R_N} \right), \end{aligned} \quad (6)$$

where

$$\begin{aligned} A_{N,M_N} &= \frac{N(N-1) + M_N^2}{2(2N+1)(2N-1)} \\ &+ \frac{N^2 + N - 3M_N^2}{2(2N+1)(2N-1)} \cos^2 \beta, \end{aligned} \quad (7)$$

and

$$\begin{aligned} B_{N,M_N} &= \frac{(N+1)(N+2) + M_N^2}{2(2N+3)(2N+1)} \\ &+ \frac{N^2 + N - 3M_N^2}{2(2N+3)(2N+1)} \cos^2 \beta. \end{aligned} \quad (8)$$

Note that we have rewritten the angular terms A_{N,M_N}, B_{N,M_N} from Ref. [51] such that they both have terms proportional to $\cos^2 \beta$. The detuning $\Delta_{v'}$ in Eq. (6) now only depends on the vibrational transition and is defined relative to the rotational transition to $N' = N + 1$. The terms L_N, R_N give the pole positions corresponding to the left and right branches and are defined as

$$L_N = N(N+1)B_v - [N(N-1)]B_{v'}, \quad (9)$$

$$R_N = N(N+1)B_v - [(N+1)(N+2) - 2]B_{v'}, \quad (10)$$

where B_v and $B_{v'}$ are the rotational constants for the vibrational levels v in $X^1\Sigma$ and v' in $b^3\Pi$, respectively.

We substitute Eqs (7)–(10) into Eq. (6) and gather terms such that the $b^3\Pi$ contribution to the polarisability has a similar form to that of Eq. (2). This yields an expression for the total lab-frame polarisability given by

$$\begin{aligned} \alpha_{N,M_N}(\beta) &= \left(\alpha_{\text{bkgd}}^{(0)} + \alpha_{\text{mod}}^{(0)}(N) \right) \\ &+ \left(\alpha_{\text{bkgd}}^{(2)} + \alpha_{\text{mod}}^{(2)}(N) \right) C_{N,M_N} P_2(\cos \beta) \end{aligned} \quad (11)$$

where

$$\alpha_{\text{mod}}^{(0)}(N) \equiv \sum_{v'} \frac{\pi c^2 \Gamma_{v'}}{2\omega_{v'}^3 (2N+1)} \left(\frac{N}{\Delta_{v'} + L_N} + \frac{N+1}{\Delta_{v'} + R_N} \right), \quad (12)$$

and

$$\alpha_{\text{mod}}^{(2)}(N) \equiv \sum_{v'} \frac{\pi c^2 \Gamma_{v'}}{2\omega_{v'}^3 (2N+1)} \left(\frac{2N+3}{\Delta_{v'} + L_N} + \frac{2N-1}{\Delta_{v'} + R_N} \right), \quad (13)$$

are the scalar and tensor modifications to the polarisability due to the transitions to the $b^3\Pi$ potential. The values of $\alpha_{\text{mod}}^{(0)}, \alpha_{\text{mod}}^{(2)}$ depend on N but not on M_N .

For simplicity, we define total scalar and tensor polarisabilities that are the sum of the background polarisability and the polarisability resulting from transitions to $b^3\Pi$

$$\tilde{\alpha}_N^{(0)} \equiv \alpha_{\text{bkgd}}^{(0)} + \alpha_{\text{mod}}^{(0)}(N), \quad (14)$$

$$\tilde{\alpha}_N^{(2)} \equiv \alpha_{\text{bkgd}}^{(2)} + \alpha_{\text{mod}}^{(2)}(N), \quad (15)$$

such that the lab-frame polarisability can be written identically to Eq. (2). This results in Eq. (1) of the main text. However, it is crucial to note that the relationship between these scalar and tensor polarisabilities and the parallel and perpendicular component does not follow that given in Eqs (3) and (4) as the rotational structure of the excited state can no longer be ignored. A full treatment in terms of the parallel and perpendicular polarisabilities is given in Ref. [47]. Finally, we note that our model ignores any hyperfine structure and Zeeman shifts in the electronically excited state.

In our implementation of this model, we include only poles resulting from transitions to $v' \leq 3$. This is because further transitions have minimal effect in the region of detuning between the transitions to $v' = 0$ and $v' = 1$. For example, the contribution from the transition to $v' = 3$ in this detuning region is $\lesssim 0.1\%$ of the total polarisability. Extended Data Table I lists all the parameters of this model, their source, and their values used or measured throughout this work. Most parameters have been independently measured and we fit only $B_{v'}$ and $\alpha_{\parallel}^{\text{bkgd}}$ when comparing our model to the experimental results.

Establishing a common detuning axis. Experimentally, we reference the detuning with respect to the unambiguously identifiable hyperfine transition ($X^1\Sigma^+, v = 0, N = 1, M_F = 6$) \rightarrow ($b^3\Pi_0, v' = 0, N' = 0, M_{F'} = 5$), at the 181.699(1) G magnetic field at which we operate. We denote this transition frequency ν^{REF} . The trap light frequency ν is accurately referenced relative to this transition (to ~ 1 kHz uncertainty) through the modes of an ultralow expansion cavity with a known free spectral range, which we also use to lock the magic-wavelength laser.

In our model of the polarisability, zero detuning for the $v' = 0$ excited state is defined as the transition from lowest rovibrational level of the electronic ground state to the manifold $N' = 1$ of $b^3\Pi$. We denote this transition frequency $\nu_{0 \rightarrow v'=0}$. We relate this to ν^{REF} using $\nu_{0 \rightarrow v'=0} \equiv \nu^{\text{REF}} + 2B_0 + 2B_{v'}$, where B_0 is the rotational constant associated with the ($X^1\Sigma^+, v = 0$) manifold, and $B_{v'}$ is the *effective* rotational constant of the ($b^3\Pi_0, v' = 0$) manifold, which we fit (see later). In the main text, we reference all trapping light frequencies ν with respect to $\nu_{0 \rightarrow v'=0}$ exclusively with the symbol Δ , where $\Delta \equiv \nu - \nu_{0 \rightarrow v'=0}$.

Fitting the light shifts

Here, we motivate the functions that we use when fitting the

$$\begin{pmatrix} I\alpha_N^{(0)} + Is(\Delta - \Delta_N^{\text{iso}})G_{aa}(\beta) & 0 & 0 \\ 0 & hf_0 + I\alpha_{N'}^{(0)} + Is(\Delta - \Delta_{N'}^{\text{iso}})G_{bb}(\beta) & Is(\Delta - \Delta_{N'}^{\text{iso}})G_{b'b}(\beta) \\ 0 & Is(\Delta - \Delta_{N'}^{\text{iso}})G_{b'b}^*(\beta) & hf_0 + \delta E + I\alpha_{N'}^{(0)} + Is(\Delta - \Delta_{N'}^{\text{iso}})G_{b'b'}(\beta) \end{pmatrix}, \quad (17)$$

in the basis $\{|a\rangle, |b\rangle, |b'\rangle\}$. The trap light couples the states $|b\rangle$ and $|b'\rangle$. These coupling terms (the off-diagonal matrix elements) are small compared to the diagonal matrix elements so the eigenstates of the system are $|a\rangle$ and the slightly dressed states $|\tilde{b}\rangle$ and $|\tilde{b}'\rangle$ with energies E_a , $E_{\tilde{b}}$, and $E_{\tilde{b}'}$ respectively. The energy $E_{\tilde{b}} - E_a$ of the dressed transition $|a\rangle \rightarrow |\tilde{b}\rangle$, to

light shifts such as those shown in Fig. 2(b). We derive these fitting functions by considering the full ac Stark Hamiltonian, and compute its effects as a perturbation to second order around the magic condition where $\tilde{\alpha}^{(2)} \approx 0$.

General lab-frame polarisability. For light polarised at an angle β to the quantisation axis, in the x-z plane, a general normalised Jones vector is $\epsilon = (\sin \beta, 0, \cos \beta)^\top$. Here, for a molecule with internuclear axis at a polar angle (θ, ϕ) to the quantisation axis, the lab-frame polarisability can be written as $\alpha(\theta, \phi, \beta) = \alpha^{(0)} + \alpha^{(2)}G(\theta, \phi, \beta)$, where

$$\begin{aligned} G(\theta, \phi, \beta) &= 2\sqrt{\frac{\pi}{5}}P_2(\cos \beta)Y_{2,0}(\theta, \phi) \\ &\quad - \frac{3}{2}\sqrt{\frac{2\pi}{15}}\sin^2(\beta)(Y_{2,2}(\theta, \phi) + Y_{2,-2}(\theta, \phi)) \\ &\quad + i\frac{3}{2}\sqrt{\frac{2\pi}{15}}\sin(2\beta)(Y_{2,1}(\theta, \phi) + Y_{2,-1}(\theta, \phi)). \end{aligned} \quad (16)$$

Here, $Y_{N,M}(\theta, \phi)$ are spherical harmonics, and $P_2(x) \equiv (3x^2 - 1)/2$ is a Legendre polynomial. Working in the spherical basis, computing the matrix elements $\langle N', M'_N | G(\theta, \phi, \beta) | N, M_N \rangle \equiv G_{N, M_N, N', M'_N}(\beta)$ involves computing integrals of the product of three spherical harmonics, known as Gaunt coefficients. For the diagonal elements, $G_{N, M_N, N, M_N}(\beta) = C_{N, M_N} P_2(\cos \beta)$.

Fitting functions. The magic condition is far from the poles of polarisability shown in Fig. 1. Therefore, to a very good approximation, near the magic condition, $\tilde{\alpha}_N^{(2)}(\Delta) \approx s(\Delta - \Delta_N^{\text{iso}})$, where s is a constant (independent of N) and Δ_N^{iso} is the detuning where $\tilde{\alpha}_N^{(2)} = 0$. Further, $\tilde{\alpha}_{N'}^{(0)}(\Delta) - \tilde{\alpha}_N^{(0)}(\Delta)$ is, to a very good approximation, a constant which we denote $\tilde{\alpha}_{N'}^{(0)} - \tilde{\alpha}_N^{(0)}$. We analyse the effect of these polarisabilities on the light shifts of a transition by considering three states $|a\rangle \equiv (N, M_N)$, $|b\rangle \equiv (N+1, M'_N)$, and $|b'\rangle \equiv (N+1, M''_N)$ in the ground electronic manifold. Here, $|a\rangle$ is a state in one rotational manifold and $|b\rangle$ and $|b'\rangle$ are two states in a different manifold with different projections of rotational angular momentum. The energies of the states in free space are 0, hf_0 , and $hf_0 + \delta E$ respectively and the microwave transition of interest is the electric-dipole allowed transition $|a\rangle \rightarrow |b\rangle$. In the near-magic trap, the Hamiltonian describing the system is

second order in intensity, is

$$\begin{aligned} E_{\tilde{b}} - E_a &\approx hf_0 \\ &\quad + s[G_{bb}(\beta) - G_{aa}(\beta)](\Delta - \Delta_{\text{magic}})I \\ &\quad + [s^2|G_{b'b}(\beta)|^2/\delta E](\Delta - \Delta_{N'}^{\text{iso}})^2I^2, \end{aligned} \quad (18)$$

where

$$\Delta_{\text{magic}} \equiv \frac{(\alpha_N^{(0)} - \alpha_{N'}^{(0)})/s + G_{bb}(\beta)\Delta_{N'}^{\text{iso}} - G_{aa}(\beta)\Delta_N^{\text{iso}}}{G_{bb}(\beta) - G_{aa}(\beta)}. \quad (19)$$

This motivates the general fitting function

$$f = f_0 + k(\Delta - \Delta_{\text{magic}})I + k'(\Delta - \Delta_{\text{iso}})^2 I^2, \quad (20)$$

that we use in the main text. As in the main text, f_0 is the frequency of the transition $|a\rangle \rightarrow |b\rangle$ in free space, k is the sensitivity constant, Δ_{magic} is the location where the first-order light shift vanishes, k' is the hyperpolarisability constant, and Δ_{iso} is the approximate detuning where the tensor light shifts are nulled. For the stretched states considered in this work, the off-diagonal terms in Eq. (17) vanish when $\beta = 0^\circ$ and we expect no hyperpolarisability, so fix $k' = 0$.

We use the Python package Diatomic-Py [52] to calculate the molecular structure of $^{87}\text{Rb}^{133}\text{Cs}$ molecules (hereafter RbCs) in the electronic ground state, including hyperfine structure. We incorporate our polarisability model by calculating $\tilde{\alpha}_N^{(0)}$ and $\tilde{\alpha}_N^{(2)}$ for each N . Then, we expand the polarisability operator for each N and diagonalise the total Hamiltonian. Predictions of δE from this model allow us to predict values of k' , which are consistent with those measured.

Experimental apparatus

Our experimental apparatus has been extensively described in previous works. Briefly, we prepare individually trapped ^{87}Rb and ^{133}Cs (hereafter Rb and Cs respectively) atoms in arrays of species-specific optical tweezers [53, 54]. We convert Rb-Cs atom pairs into RbCs molecules in the absolute ground state with a combination of magnetic-field ramps and laser pulses [36, 46, 55].

The optical tweezers which trap the atoms and molecules are formed by focusing light with a high numerical-aperture objective lens which is outside the vacuum chamber in which the experiments take place. The experiments in this work are performed after we transfer the RbCs molecules to an array of magic-wavelength tweezers formed from light at wavelength $\sim 1145.3\text{ nm}$ [21]. The tweezers in this array have $1/e^2$ waists of $1.76(4)\mu\text{m}$ and, unless stated otherwise, we use a trap-centre intensity $I = 4.6(3)\text{ kW/cm}^2$. We form this array from a common source by deflecting light prior to the objective lens with an acousto-optic modulator (AOM). We drive this AOM with multiple radio-frequency (RF) tones simultaneously. Each RF tone causes an additional beam to be diffracted from the AOM. This diffraction means that each trap is formed from light at a slightly different frequency; we use this to increase our rate of data acquisition. We prepare arrays of up to four molecules, each in their own trap. This allows us to measure the effect of four different detunings Δ spanning $\sim 30\text{ MHz}$ at once (e.g. for the measurement shown in Fig. 2).

Controlling the polarisation of the tweezers. In the main text we characterise the effect that the polarisation of the tweezer light has on the magic trapping condition. We set this polarisation by changing the polarisation of the light that forms the tweezers prior to the objective lens. First, we use a polariser to ensure that the light is linearly polarised. We then pass the light through the AOM which forms the multiple traps. We use a zero-order half-wave plate after the AOM to set the angle of the linear polarisation.

However, the light then passes through several polarisation-dependent optics before the molecules: two large dichroic mirrors (to overlap the magic-wavelength tweezers with the other tweezers in our apparatus [36, 53]), a large mirror beneath the objective lens, the objective lens itself, and

the glass of the vacuum chamber. Additionally, the traps in the array have slightly different angles of incidence onto the lenses in the optical setup. Therefore, we expect that the polarisation angle at the molecules (β) could be slightly different to our measured value. Additionally, we expect there could be a small polarisation gradient across the array, as observed in similar experiments [56]. We neglect small changes in polarisation caused by the tight focussing of the tweezers [54, 57–59]. For each measured transition, the polarisation remains constant and any resulting error is systematic. The estimated magnitude of these systematic deviations are discussed later.

Driving rotational transitions. We drive transitions between rotational states in the ground manifold ($X^1\Sigma^+, v = 0$) with microwave radiation [36]. Allowed electric-dipole transitions are those that satisfy $|\Delta N| = \pm 1$ and $|\Delta M_N| \leq 1$. We drive all the transitions studied using a dipole Wi-Fi antenna which is mounted outside the vacuum chamber. Magnetic-field coils around the vacuum chamber mean that we do not have good control of the microwave polarisation at the molecules. Therefore, to prevent unwanted off-resonant driving of other hyperfine transitions, we limit the microwave Rabi frequencies to $\sim 10\text{ kHz}$. We are then able to coherently transfer molecules from the absolute ground state $(0, 0)$ to the excited rotational states $(1, 1)$ and $(2, 2)$.

Tweezer-intensity noise. The primary limitation to rotational coherence times in our experiment is noise on the intensities of the magic-wavelength tweezers [21]. To analyse the effect of this noise, we assume that during repeats of the experiment the tweezer intensities are sampled from a Gaussian distribution with mean I and standard deviation σ_I . For experiments performed when $\beta = 0^\circ$ (e.g. those in Fig. 4), this is mapped to transition-frequency noise $\sigma = k\sigma_I(\Delta - \Delta_{\text{magic}})$. This causes decoherence between experimental repeats, such that there is Gaussian decay in the Ramsey contrast $C(T) = e^{-(T/T_2^*)^2}$, where T is the hold time and $T_2^* = \sqrt{2}/(2\pi\sigma)$ is the coherence time [60]. From the data in Fig. 4, we fit $\sigma_I/I = 0.65(5)\%$. This is consistent with ex-situ measurements of the tweezer powers and prior characterisations using only two molecular levels [21]. At our usual trapping intensity of $4.6(3)\text{ kW/cm}^2$, we expect $T_2^* > 1.5\text{ s}$ for all considered superpositions when using the optimal detuning indicated by the grey line in Fig. 4.

Magnetic- and electric-field noise. When the molecules are trapped in the magic-wavelength tweezers, we expect that the next limitation on achievable coherence times is noise on the magnetic and electric fields in our apparatus. Extended Data Table II gives the magnetic- and electric-field sensitivities of the transitions within the ground manifold ($X^1\Sigma^+, v = 0$) that we study in this work. These are calculated with Diatomic-Py [52]. We work with stretched rotational states; this means that the magnetic sensitivities are constant with magnetic field. The largest magnetic-field sensitivity is that of the two-photon transition $(0, 0) \rightarrow (2, 2)$ which has a frequency shift of 9.46 Hz/G . We have measured $\sim 20\text{ mG}$ magnetic-field noise using Rb hyperfine transitions. This level of noise would limit the coherence time to $\sim 5\text{ s}$. The largest electric-field sensitivity is also that of the two-photon transition $(0, 0) \rightarrow (2, 2)$ which experiences a frequency shift of -13 mHz/(mV/cm) . This sensitivity is calculated at a

bias field of 60 mV/cm which we have measured using spectroscopy of Rydberg levels in Rb atoms. The electric-field noise in our apparatus is ~ 2 mV/cm which is sufficiently low that it bounds the coherence time to tens of seconds.

Molecule lifetimes. Molecular lifetimes are limited by Raman scattering of the trapping light from the molecules. When a Raman scattering event occurs, the molecules are lost to a different internal state which we do not detect with our multistate readout scheme [21, 36]. This results in apparent molecule loss and we correct for these errors with postselection. Extended Data Figure 1(a) shows the loss for the three rotational states that we use in this work at a trapping intensity $I = 8$ kW/cm². We do not expect the loss rate to depend on the rotational state, and we fit a lifetime of 3.7(3) s. Extended Data Figure 1(b) shows that the loss rate for the state (0, 0) varies with I with a fitted intensity-dependent loss rate of $0.17(1) \text{ s}^{-1}/(\text{kW}/\text{cm}^2)$.

Measuring molecular polarisability

We realise the magic trapping condition by tuning α_{\parallel} whilst α_{\perp} remains approximately constant (i.e. close to its background value $\alpha_{\perp}^{\text{bkgd}}$) [31]. Near the magic-trapping condition, the overall lab-frame polarisability α_N is effectively isotropic ($\alpha_{\parallel} \simeq \alpha_{\perp}^{\text{bkgd}}$), hence $\alpha_N \simeq \alpha_{\perp}^{\text{bkgd}}$. We measure $\alpha_{\perp}^{\text{bkgd}}$ by comparing the polarisability of RbCs in the state (0, 0) to the known value of the polarisability of a Cs atom in the same trap. The polarisability of Cs is $\alpha_{\text{Cs}} = 919(3) \times 4\pi\epsilon_0 a^3$ at 1145.3 nm [61]. The polarisability of RbCs compared to Cs is

$$\alpha_{\text{RbCs}} = \alpha_{\text{Cs}} \frac{m_{\text{RbCs}}}{m_{\text{Cs}}} \left(\frac{f_{\text{RbCs}}}{f_{\text{Cs}}} \right)^2, \quad (21)$$

where m_i is the mass and f_i is the trap frequency for species $i = \{\text{RbCs}, \text{Cs}\}$. We measure the trap frequencies with parametric heating [62] and compare them to obtain $f_{\text{RbCs}}/f_{\text{Cs}} = 0.704(7)$. From this we extract the polarisability $\alpha_{\text{RbCs}} = \alpha_{\perp}^{\text{bkgd}} = 754(18) \times 4\pi\epsilon_0 a^3 = 35.3(8) \text{ Hz}/(\text{W}/\text{cm}^2)$. This is in reasonable agreement with the theoretical prediction of Guan *et al.* ($34 \text{ Hz}/(\text{W}/\text{cm}^2)$) [30].

Finding the magic condition

For each rotational transition that we study, we perform Ramsey spectroscopy to identify the magic trapping condition. For the one-photon transitions (0, 0) \rightarrow (1, 1) and (1, 1) \rightarrow (2, 2), we initialise the molecules in the lower-energy state and perform a $\pi/2$ pulse on the transition with near-resonant microwaves (detuned by ~ 300 Hz). We wait for a hold time T before performing another $\pi/2$ pulse. This pulse maps the phase that accumulates between the two states onto the state populations, which oscillate at the detuning of the microwaves from the bare transition [e.g. as in Fig. 2(a)].

When interrogating the two-photon transition (0, 0) \rightarrow (2, 2), we first initialise the molecules in the state (0, 0). We apply a $\pi/2$ pulse on the transition (0, 0) \rightarrow (1, 1) then a π pulse on the transition (1, 1) \rightarrow (2, 2). Both microwave pulses are detuned from the one-photon transitions by ~ 150 Hz. We wait for a time T , then invert the pulse sequence, here Ramsey fringes occur at the two-photon detuning.

Fitting two-level fringes. After the two-level Ramsey sequences, the population of the states takes the general form

$$(1 + C \cos(2\pi fT + \phi))/2, \quad (22)$$

which we fit to the data. Here, C is the fringe contrast, f is the frequency of the fringes, and ϕ is a phase shift of the fringes, typically fixed to $\phi = \pi$. The sensitivity of the phase of the Ramsey fringe with respect to f scales linearly with T . For example, assuming a 10% error in resolving the phase (modulo 2π) to achieve a Hz-level error requires measuring Ramsey fringes out to $T \sim 100$ ms.

We circumvent the need to measure all times out to ~ 100 ms by measuring blocks of fringes separated in time. However, this method forms a very multimodal posterior distribution for f . Most error minimisation solvers fail to find the correct mode, or assign correct probabilities to each mode. For this reason, we use the nested sampling Monte Carlo algorithm MLFriends [63] using the UltraNest package [64] to derive the posterior probability distributions for f and assign confidence intervals. We generally minimise the probability weight assigned to other modes by measuring extra fringe blocks at $T/2$, $T/3$, and $T/5$.

Extracting the magic detunings. For the measurements of the transition frequencies, such as those shown in Fig. 2(b), we fit the data $f(\Delta, I)$ with Eq. (20). We fix $k' = 0$ when $\beta = 0^\circ$ as we do not expect hyperpolarisability. For the measurements taken with $\beta = 90^\circ$, we fix $\Delta_{\text{iso}} = 185.47 \text{ GHz}$, 185.53 GHz , 185.60 GHz for the transitions (0, 0) \rightarrow (1, 1), (1, 1) \rightarrow (2, 2), and (0, 0) \rightarrow (2, 2) respectively, when fitting k' . This is because we have insufficient data to fit both Δ_{iso} and k' simultaneously. These values are informed by the measurements taken with $\beta = 0^\circ$ and the results in Ref. [31], which we fit to our polarisability model.

To account for any site-to-site variations in our tweezer array, we independently fit our model for each tweezer site. We report the parameter values as the mean of the fitted parameters, with the errors given by the standard deviation across all four sites. For superpositions and tweezer polarisations where Δ_{magic} is most sensitive to changes in β (see Eq. (19) and Fig. 3), we note a marked difference in the detuning of the magic condition site to site. We attribute these shifts to varying polarisation across the array. As an example, Extended Data Fig. 2(a) displays the frequency f of the transition (1, 1) \rightarrow (2, 2) against I for various detunings Δ . For this data, $\beta = 90^\circ$. Each panel shows the data for different sites in the tweezer array. Each site displays hyperpolarisability, but the extracted magic detuning for each site is different, as shown in Extended Data Fig. 2(b). The grey error bar below is the mean and standard deviation of the set of Δ_{magic} for each site; this is the value we report in Fig. 3.

Extended Data Table III summarises the fit parameters that we extract for each transition and polarisation when averaging across the tweezer array. In Extended Data Fig. 3, we show the dependence of Δ_{magic} on β for each transition. We estimate the polarisation gradient across the tweezer array, by assuming a mapping from the polarisation angle we measure on the optical table (β') to the polarisation angle at the molecules (β) of the form $\beta = \beta' + (4 - i)(\delta\beta) + (\Delta\beta)$. Here, $\delta\beta$ is the site-to-site change in polarisation, i is the index of the site, and $\Delta\beta$ is the gross change in polarisation referenced to site $i = 4$. We estimate these shifts to be $\delta\beta \sim -1^\circ$ and $\Delta\beta \sim -2^\circ$. We attribute this polarisation gradient primarily to axial misalignment of the $4f$ telescope which expands the tweezer light prior to the objective lens, as was the case for the experiment in Ref. [56].

Fitting the molecular constants. As described in the main

text, we use the measured values of Δ_{magic} and k to fit our model of the molecular polarisability (see the lines in Fig. 3). As already noted, the majority of the parameters in our model are fixed to the molecular constants in Refs [35, 37] and the independently measured value of $\alpha_{\perp}^{\text{bkgd}}$ (see above). The remaining two parameters, which we fit, are the effective rotational constant of the excited state $B_{v'} = 518.0(4)$ MHz and the background parallel polarisability $\alpha_{\parallel}^{\text{bkgd}} = 134.4(8)$ Hz/(W/cm²).

Three-level Ramsey sequence

In the main text, we describe a Ramsey sequence which we generalise to a three-level system. First, we generate an equal superposition of the three states $(0, 0)$, $(1, 1)$, and $(2, 2)$. We initialise the molecules in the state $(0, 0)$ and then perform a $2 \cos^{-1}(1/\sqrt{3})$ -radian pulse on the transition $(0, 0) \rightarrow (1, 1)$, followed by a $\pi/2$ pulse on the transition $(1, 1) \rightarrow (2, 2)$. As in the two-level Ramsey procedure, these states accumulate relative phases during the Ramsey hold time T . After this hold time, we perform a sequence of $\pi/2$ pulses. First, we drive the transition $(0, 0) \rightarrow (1, 1)$, then the transition $(1, 1) \rightarrow (2, 2)$, and finally the transition $(0, 0) \rightarrow (1, 1)$ again (see Fig. 5). This sequence causes non-trivial interference in the populations of the three states.

We derive the interference pattern by analytically propagating a pure state through each of the pulses, assuming there is no decoherence or transition drifts. For the sake of simplicity, here we treat the pulses as ideal and assume that the one-photon detunings δ_{01}, δ_{12} are much less than the one-photon Rabi frequencies Ω_{01}, Ω_{12} . Immediately after the Ramsey hold time T , the molecules are in the state

$$|\psi(\delta_{01}, \delta_{12}, T)\rangle = \frac{1}{\sqrt{3}}(|0\rangle + e^{2\pi i \delta_{01} T} |1\rangle + e^{2\pi i (\delta_{01} + \delta_{12}) T} |2\rangle), \quad (23)$$

where $|0\rangle \equiv (0, 0)$, $|1\rangle \equiv (1, 1)$, and $|2\rangle \equiv (2, 2)$. After the pulse sequence, the populations of the states are

$$P_0 = \frac{1}{12} \left(4 - \cos 2\pi \delta_{01} T + (-2 - \sqrt{2}) \cos 2\pi \delta_{12} T + (2 - \sqrt{2}) \cos 2\pi (\delta_{01} + \delta_{12}) T \right), \quad (24)$$

$$P_2 = \frac{1}{6} \left(2 + \cos 2\pi \delta_{01} T + \sqrt{2} \cos 2\pi \delta_{12} T + \sqrt{2} \cos 2\pi (\delta_{01} + \delta_{12}) T \right), \quad (25)$$

and $P_1 = 1 - P_0 - P_2$, which we use to fit the interference fringes. Again, due to the non-trivial χ^2 surface, we fit using the package described in Ref. [64].

Quantum Fisher information. The quantum Fisher information matrix for a pure state $|\psi(\vec{p})\rangle$ which is parameterised by $\vec{p} = (p_1, p_2, \dots)$ is given by

$$\mathcal{F}_{ab} = 4 \text{Re} (\langle \partial_a \psi | \partial_b \psi \rangle - \langle \partial_a \psi | \psi \rangle \langle \psi | \partial_b \psi \rangle), \quad (26)$$

where a, b are indices of parameters in \vec{p} [33]. The quantum

multiparameter Cramér–Rao bound is given by

$$\text{Cov}(\vec{p}) \geq \frac{1}{n} \mathcal{F}^{-1}, \quad (27)$$

where $\text{Cov}(\cdot)$ indicates the covariance matrix of the parameters, and n is the number of experimental repetitions [33].

Between the $\pi/2$ pulses of an ideal two-level Ramsey sequence connecting states i and j , the state is given by $|\psi(\delta_{ij}, T)\rangle = (|i\rangle + e^{2\pi i \delta_{ij} T} |j\rangle)/\sqrt{2}$. The quantum Fisher information of δ_{ij} for this state is then given by $\mathcal{F} = (2\pi T)^2$, which implies $\text{Var}(\delta_{ij}) \geq 1/(n(2\pi T)^2)$. For the three-level state in Eq. (23), the quantum Fisher information matrix is given by

$$\begin{pmatrix} \frac{8}{9}(2\pi T)^2 & \frac{4}{9}(2\pi T)^2 \\ \frac{4}{9}(2\pi T)^2 & \frac{8}{9}(2\pi T)^2 \end{pmatrix}. \quad (28)$$

Inverting this matrix, the Cramér–Rao bound states $\text{Var}(\delta_{01}), \text{Var}(\delta_{12}) \geq (3/2)/(n(2\pi T)^2)$. Therefore, we would require $\text{Var}(\delta_{12})/(2 \text{Var}(\delta_{ij})) = (3/2)/2 = 3/4$ times as many measurements in the three-level case to achieve the same variance bound as two individual two-level Ramsey sequences for a projective measurement that saturates the Cramér–Rao bound. Note that the optimal projective measurement can be dependent on the parameters one is trying to measure (as is the case in general for multiparameter estimation problems), and requires complicated adaptive measurement protocols to continually saturate the Cramér–Rao bound [65]. Removing the final $\pi/2$ pulse on the transition $(0, 0) \rightarrow (1, 1)$ produces an interferometer that at intermittent times T , fully saturates the Cramér–Rao bound. This however, would be at the expense of not directly seeing preservation of all coherences in all state populations.

Data availability

The data that support the findings of this study are available at <https://doi.org/10.15128/r2kk91fk55v>.

Acknowledgments

We thank Arpita Das, Albert Li Tao, and Luke M. Fernley for sharing their spectroscopy results and Luis Santos and Ana Maria Rey for useful discussions. We acknowledge support from the UK Engineering and Physical Sciences Research Council (EPSRC) Grants EP/P01058X/1, EP/V047302/1, and EP/W00299X/1, UK Research and Innovation (UKRI) Frontier Research Grant EP/X023354/1, the Royal Society, and Durham University.

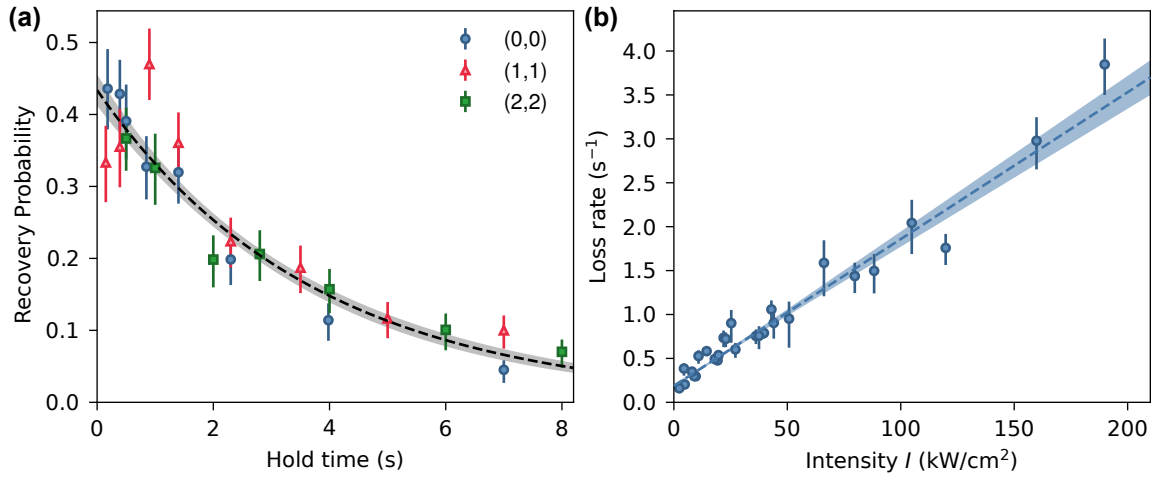
Author contributions

T.R.H. and D.K.R. performed the experiments with support from A.G. and F.v.G.; T.R.H. analysed the data with assistance from P.D.G. and D.K.R.; T.R.H. wrote the original draft of the paper and all authors reviewed and edited it; S.L.C. supervised the work and managed funding acquisition.

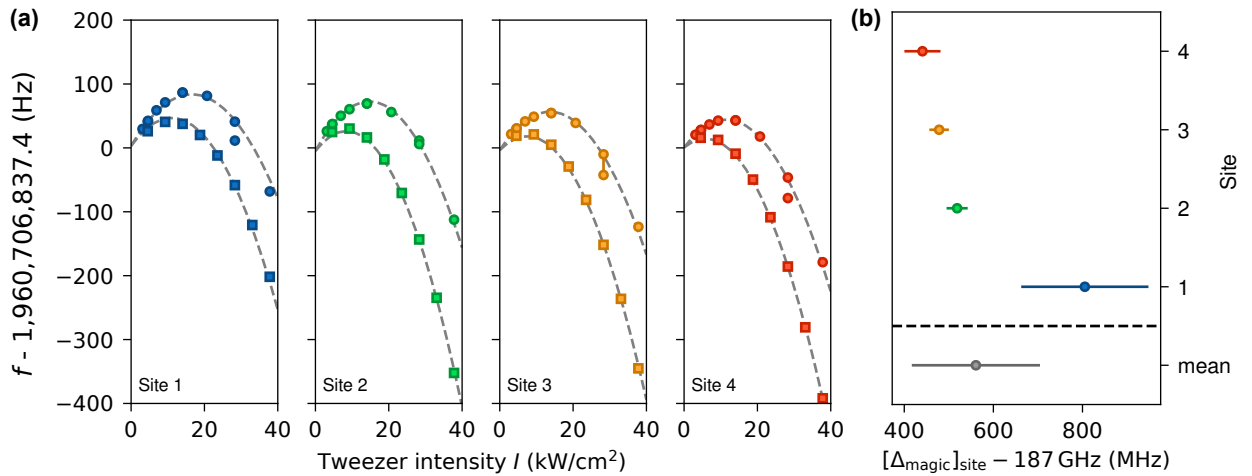
Competing interests

The authors declare no competing interests.

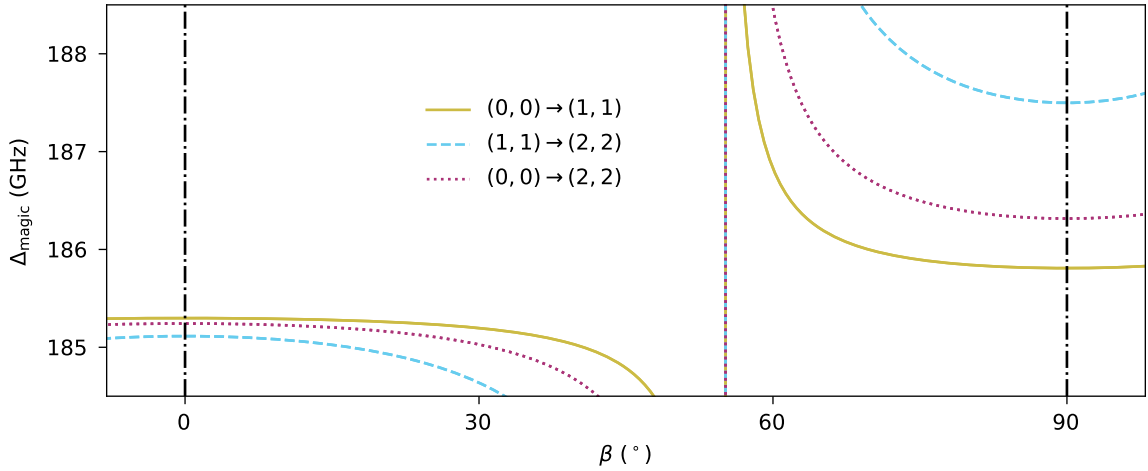
Correspondence and requests for materials should be addressed to Simon L. Cornish.



Extended Data Fig. 1. **Lifetimes of molecules in the magic-wavelength tweezers.** (a) Probability of recovering molecules in the states (0,0) (blue circles), (1,1) (red triangles), and (2,2) (green squares) for varying hold times at a tweezer intensity of $I = 8 \text{ kW/cm}^2$. An exponential decay model (solid line) is fitted to the data and the 1σ uncertainty on the model is shown as the shaded region. (b) Extracted loss rates for different tweezer intensities I for molecules in the state (0,0). A linear model (solid line) is fitted to the data, with 1σ uncertainty shown as the shaded region. Error bars in all panels are 1σ confidence intervals.



Extended Data Fig. 2. **Site-to-site variations in the magic-trapping condition across the tweezer array.** (a) Transition frequencies for the transition $(1,1) \rightarrow (2,2)$ with $\beta = 90^\circ$, for each site of the tweezer array, showing hyperpolarisability. (b) The independent fits of Δ_{magic} for each site with their statistical errors. The grey error bar separated below represents the value and error we quote, from the mean and standard deviation of the fitted values for each site.



Extended Data Fig. 3. **Effect of tweezer polarisation on the magic detunings.** The magic detuning (Δ_{magic}) predicted by our model (Eq. (19)) is plotted as a function of the polarisation angle (β) for the transitions indicated in the legend. The black vertical lines indicate $\beta = 0^\circ$ and $\beta = 90^\circ$.

Extended Data Table I. **Values and sources of the parameters in our model.**

Parameter	Value	Source
B_0	490.173 994(45) MHz	[66]
$B_{v'}$	518.0(4) MHz	This work; fit to our model.
$\alpha_{\perp}^{\text{bkgd}}$	35.3(8) Hz/(W/cm ²)	This work; parametric heating measurements.
$\alpha_{\parallel}^{\text{bkgd}}$	134.4(8) Hz/(W/cm ²)	This work; fit to our model.
$\omega_{v'=0}$	261.569 87(6) THz	[35]
$\Gamma_{v'=0}$	14.1(3) kHz	[35]
$\omega_{v'=1}$	$\omega_{v'=0} + 1493.782\,274(2)$ GHz	[35]
$\Gamma_{v'=1}$	8.1(3) kHz	[35]
$\omega_{v'=2}$	$\omega_{v'=0} + 2983.743\,109(2)$ GHz	[35]
$\Gamma_{v'=2}$	1.44 kHz	[30]
$\omega_{v'=3}$	$\omega_{v'=0} + 4469.882\,54(2)$ GHz	[35]
$\Gamma_{v'=3}$	0.206 kHz	[30]

Extended Data Table II. **Sensitivities of rotational-transition frequencies in the ground manifold ($X^1\Sigma^+, v = 0$) to external magnetic and electric fields.** The sensitivities are calculated with Diatomic-Py [52]. We calculate the electric-field sensitivities assuming a bias field of 60 mV/cm.

Transition	Magnetic-field sensitivity (Hz/G)	Electric-field sensitivity (mHz/(mV/cm))
(0, 0) \rightarrow (1, 1)	4.73	-10.9
(1, 1) \rightarrow (2, 2)	4.73	-2.44
(0, 0) \rightarrow (2, 2)	9.45	-13.3

Extended Data Table III. **Fitted parameters of the transitions as described in the main text.**

β	Transition	f_0 (Hz)	k (mHz/MHz/(kW/cm ²))	Δ_{magic} (GHz)	$k'(\Delta_{\text{magic}} - \Delta_{\text{iso}})^2$ (mHz/(kW/cm ²) ²)
0°	(0, 0) \rightarrow (1, 1)	980,385,597.3(2)	98(3)	185.2980(7)	-
	(1, 1) \rightarrow (2, 2)	1,960,706,837.3(2)	38(2)	185.142(3)	-
	(0, 0) \rightarrow (2, 2)	2,941,092,437(3)	184(11)	185.239(5)	-
90°	(0, 0) \rightarrow (1, 1)	980,385,598.3(6)	-43(2)	185.86(2)	25(2)
	(1, 1) \rightarrow (2, 2)	1,960,706,837(4)	-18(3)	187.54(11)	-580(50)
	(0, 0) \rightarrow (2, 2)	2,941,092,440(3)	-63(4)	186.36(3)	26(2)